www.czasopisma.pan.pl PAN POLSKA AKADEMIA NAUK www.journals.pan.pl

Arch. Metall. Mater. **63** (2018), 2, 1019-1029

DOI: 10.24425/122437

P.K. CHAURASIA*, C. PANDEY*#, A. GIRI*, N. SAINI*, M.M. MAHAPATRA*

A COMPARATIVE STUDY OF RESIDUAL STRESS AND MECHANICAL PROPERTIES FOR FSW AND TIG WELD ON STRUCTURAL STEEL

Mechanical properties and residual stresses of friction stir welded and autogenous tungsten inert gas welded structural steel butt welds have been studied. Friction stir welding (FSW) of structural steel butt joints has been carried out by in-house prepared tungsten carbide tool with 20 mm/ min welding speed and 931 rpm tool rotation. Tungsten inert gas (TIG) welding of the butt joints was carried out with welding current, arc voltage and the welding speed of 140 amp, 12 V and 90 mm/min respectively. Residual stress measurement in the butt welds has been carried out in weld fusion zone and heat affected zone (HAZ) by using blind hole drilling method. The magnitude of longitudinal residual stress along the weld line of TIG welded joints were observed to be higher than friction stir welded joint. In both TIG and FSW joints, the nature of longitudinal stress in the base metal was observed to be compressive whereas in HAZ was observed to be tensile. It can be stated that butt welds produced with FSW process had residual stress much lower than the autogenous TIG welds.

Keywords: FSW, TIG, Residual stress, Microstructure, Hardness

1. Introduction

Residual stresses are self-equilibrating stresses which exist in elastic bodies as the response to uneven plastic strains. Origin of residual stresses in an engineering component is a consequence of combined interaction of thermal loading , deformation and material microstructure [1].

The methods of residual stresses measurement can be broadly categorized into three types: destructive, semi-destructive and non-destructive. The destructive and semi- destructive methods of residual stress measurement are more accurate as compared to the non-destructive methods. The destructive and semi destructive methods are mechanical methods which analyze the stress-relaxation that occurs when a small volume of material is removed from a stressed metal part [2].

The strain gauge method of blind hole drilling determines stress near the surface of an isotropic linear-elastic material. In this measurement method, strain gauge rosette is paste to the stressed surface followed with drilling a hole at the geometric center of rosette. The relieved strains due to hole drilling are then measured. It measures stresses locally which indicate the residual stress within the boundaries of drilled hole. Local yielding is possible due to stress concentration around the drilled hole [3-4].

FSW is a variant of solid-state joining processes, which has been developed by The Welding Institute (TWI) in 1991, primarily for aluminum alloys. In FSW, a rotating cylindrical shouldered tool plunges into the butted plates and locally plasticizes the joint region during its movement along the joint line that result a joint beteweeen the workpieces. In FSW, the heat is mainly derived from the friction between the work material and rotating welding tool with shoulder and the probe [5].

Chen et al. [5] presented a paper on finite element modeling of FSW which dealt with thermomechanical analysis of aluminum alloy and observed that longitudinal residual stress was much higher than the lateral residual stress. Hu et al. [6] opined that application of appropriate mechanical tensioning during welding reduced the residual stress and even changed the residual stresses pattern from tensile state to compressive state. Thus, fatigue resistance and stress corrosion of the joints produced by FSW improved. Fratini et al. [7] stated that butt joint has lower residual stress in comparison with T and lap joint produced by FSW process. Milan et al. [8] investigated the patterns of residual stresses generated during FSW of aluminum alloy, according to which the peak longitudinal residual stresses were located in the thermo-mecanically heat affected zones of the advancing side of the weld, ranging from 50% to 60% of the yield strength of the parent material. Sharma et al. [9] observed fine ferrite and martensite in stir zone and higher hardness in weld zone of FSW of structural steel. Lienert et al. [10] presented a paper on friction stir welding studies on mild steel which discussed process results, microstructures and mechanical properties. Boumerzoug et al. [11] investigated the effect of fusion welding on microstructure and mechanical

* INDIAN INSTITUTE OF TECHNOLOGY ROORKEE, DEPARTMENT OF MECHANICAL AND INDUSTRIAL ENGINEERING UTTRAKHAND-247667, INDIA.

Corresponding author: chandanpy.1989@gmail.com, chandan.pndy@rediff.com

properties of industrial low carbon steel. Pasupathy et al. [12] have done detailed study on dissimilar welding of low carbon steel withAA1050 using TIG welding. The FSW is a solid-state joining process with many advantages over arc welding processes such as TIG. However, no systematic comparative study seems to have been reported in the literature on the effects of TIG and FSW process on microstructure, mechanical properties and residual stress of structural steel butt welds.

2. Material and experimental details

Structural steel was used for the present experimental work. The chemical composition of as-received structural steel was analyzed by using an optical emission spectrometer (Make: Metavision, model: 1008i), as shown in Table 1.

TABLE 1

Chemical composition of as-received structural steel

Element	Chemical composition (wt %)								
	C	Mn	Si	P	S	Ni	Al	Cr	Fe
Base metal	0.19	0.55	0.22	0.09	0.02	0.01	0.01	0.00	Rest

Friction stir welded butt joints have been produced from 3 mm thick structural steel plates by friction stir welding (FSW) process. The welding parameters are depicted in Table 2. The welding was performed along the joint line of square plates of dimension 150 mm × 50 mm × 3 mm. A compressed air flow was used in all the experiments for cooling of the upper portion of tool because tool became red hot during welding. So, for FSW of structural steel, a non-consumable tungsten carbide tool was used due to its high refractoriness, toughness and hardness (1650 HV).

TABLE 2

Welding parameters of friction stir welding

S. No.	Parameter	Welding condition
1	Welding machine	FSW
2	Welding speed (mm/min)	20
3	Rotational speed (rpm)	931
4	Tool probe profile	Conical
5	Tool tilt angle	2^0
6	Tool shoulder diameter (mm)	23
7	Pin diameter (mm)	7 & 4 (maximum and minimum)
8	Pin length (mm)	2.7

The autogenous tungsten inert gas (TIG) welded butt joints were produced of same material of thickness 3 mm. A single autogenous root pass was used to make the butt-joint. The plate dimension was 150 mm × 50 mm × 3 mm. The welding process parameters during TIG are tabulated in Table 3. To ensure the defect free weld, the joint was inspected by using the ultrasonic non-destructive testing.

TABLE 3

Welding parameters of TIG welding

S. No.	Welding parameters	Welding condition
1	Welding machine	Automatic GTAW
2	Welding speed (mm/min)	90
3	Welding current (Amp)	140
4	Welding voltage (Volts)	12
5	Inert gas used	Argon
6	Inert gas pressure (litre/min)	10
7	Plate to electrode tip distance (mm)	3
8	Diameter of thoriated tungsten electrode (mm)	3
9	Net heat input (kJ/mm)	0.84

ASTM E837 standard was used for residual stress measurement by using the blind hole drilling. Residual stress was measured by a three element strain gauge rosette FRS-2-11 at different places at weld center line of friction stir welded plates and TIG welded plates, heat affected zone of TIG welded plates and base metal portion of FSWed plates. For weld fusion zone, residual stress was measured at the center of weld for both TIG and FSWed plate while in HAZ, stress was measured to be 2 mm away from the weld fusion boundary. The material properties of base material were measured by using the tensile tester which depicts yield strength (σ_y), Young's modulus (E) and poison's ratio (μ) of 300 MPa, 210 GPa and 0.3, respectively. In this present investigation, strain gauge rosette FRS-2-11 and two single element strain gauge FLA-5-11 were used for blind hole drilling test and for longitudinal strain relaxation respectively. The gauge description is shown in Table 4. For calibration purpose, tensile test specimen was prepared. The model and actual specimen for this test are shown in Fig. 1(a) and (b) respectively in which strain gauge 3, 4 and 5 were placed longitudinally to measure strain and strain gauge 1 was placed for recording transverse strain. Strain gauge 2 was placed at 225° from reference (strain gauge element 1). Three element TML make strain gauge rosette FRS-2-11 having 2 mm hole diameter was used. Before drilling 2 mm blind hole, uniaxial tensile load was applied in several stages up to 90% of work material's yield strength. Gauge element 3 was in loading direction. Further, during loading, respective strains were recorded at each load interval. After that, a small hole of 2 mm is produced at the geometric center of strain gauge rosette FRS-2-11 up to the depth of 2 mm. After that, uniaxial load was applied in the same previous manner up to the 90% of yield strength and strains corresponding to all elements were recorded.

TABLE 4

Description of strain gauges used

	FRS -2-11 (three element)	FLA -5-11 (single element)
Gauge factor	2.07	2.13
Gauge length (mm)	1.5	5

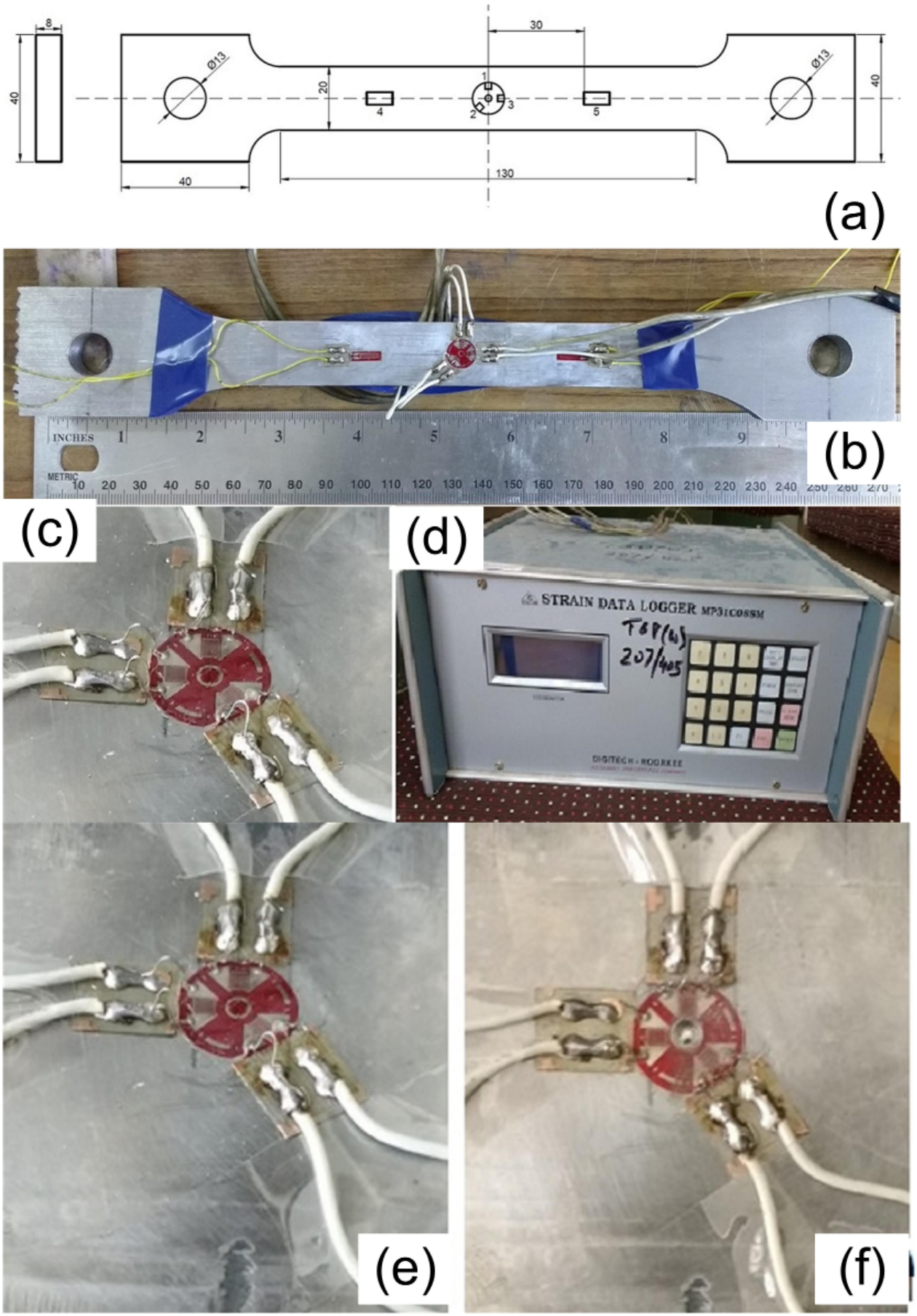

Fig. 1. Tensile specimen for plasticity test and error measurement (a) schematic (1, 2 and 3: strain gauge rosette elements, 4 and 5: single element strain gauge), (b) specimen with strain gauge rosette, (c) Three element strain gauge rosette after pasting and making terminal, (d) strain data logger; Pasted strain rosette over weld fusion zone of TIG (e) before drilling (f) after drilling condition

The principal stresses and their orientation are given in equation below [12]:

$$\sigma_{\max} = \frac{\varepsilon_1 + \varepsilon_3}{4\bar{A}} - \frac{1}{4\bar{B}}\sqrt{(\varepsilon_3 - \varepsilon_1)^2 + (\varepsilon_3 + \varepsilon_1 - 2\varepsilon_2)^2} \quad (1)$$

$$\sigma_{\min} = \frac{\varepsilon_1 + \varepsilon_3}{4\bar{A}} + \frac{1}{4\bar{B}}\sqrt{(\varepsilon_3 - \varepsilon_1)^2 + (\varepsilon_3 + \varepsilon_1 - 2\varepsilon_2)^2} \quad (2)$$

$$\tan 2\alpha = \frac{(\varepsilon_3 + \varepsilon_1 - 2\varepsilon_2)}{(\varepsilon_3 - \varepsilon_1)} \quad (3)$$

where, ε_1, ε_2 and ε_3 are the recorded strain readings in three element strain gauge rosette. The $\sigma_{\max}$ and $\sigma_{\min}$ are maximum and minimum principal stresses and α is the angle between minimum principal stress and element 1. The calibration coefficients $\bar{A}$ and $\bar{B}$ given in equation (1) and (2) depends upon geometry of strain rosette, hole depth, diameter of hole, applied load etc. The coefficients are calculated by using equations (4) and (5) in which ε_{1cal} and ε_{3cal} are the differences in strain readings in element 1 and 3 obtained from tensile testing before and after blind hole drilling. Calibration constants a and b represent the relieved strains due to unit stresses within hole depth which are calculated by the equations (6) and (7) [12]. Both are dimensionless constants for isotropic stresses and shear stresses respectively.

$$\bar{A} = \frac{\varepsilon_{1cal} + \varepsilon_{3cal}}{2\sigma_{app}} \quad (4)$$

$$\bar{B} = \frac{\varepsilon_{3cal} - \varepsilon_{1cal}}{2\sigma_{app}} \quad (5)$$

$$\bar{A} = -\frac{(1+\mu)a}{2E} \quad (6)$$

$$\bar{B} = -\frac{b}{2E} \quad (7)$$

To measure the residual stress, the weld fusion zone and HAZ is polished by emery paper up to grit size 600 because surface flaws may affect the strain relaxation readings. After cleaning by acetone, three element strain gauge rosette was pasted on the surface and terminals were prepared as shown in Fig. 1(c). After making terminals, wires were connected to a multichannel static strain indicator shown in Fig. 1(d). Plates were clamped during drilling due to which some stress were also induced and strains are recorded for the clamping effect. In the calculation of residual stresses, clamping effect was considered.

The depth of drill is measured by LVDT (linear variable displacement transducer), setting zero at the surface of plates. After drill up to 2 mm, final longitudinal and transverse strains were subtracted from initial one with considering the clamping effect also. The nature of residual stress is calculated according to calibration test of base material. Fig. 1(e) and (f) shows before and after drill with 2 mm depth condition of strain gauge rosette. For measuring residual stress in HAZ of TIG welded plate, three element strain gauge rosette was placed at 3 mm distance from fusion line. Similarly, experiment was performed on weld zone of friction stir welded butt joint.

The Vickers hardness measurement of base metal and weldment (FSW and TIG weld) was carried out on Vickers hardness tester (Omnitech-S. Auto) at the load of 500 g and dwell time of 10 sec. Metallographic samples were prepared from welds transversely using standard procedure and etched with a 5% nital solution (5% Nitric acid volume wise in Ethanol). The optical micrographs of samples were captured by CARL ZEISS lenses with software Axiovision. For phase detection in various zones of both butt welds, X-ray diffraction (XRD) analysis has been done on D-8 Bruker AXS diffractometer. It was carried out by using Cu-K_α irradiation with the working voltage and current of 40 kV and 30 mA respectively. To conduct the static-tensile test for both as-received material and specimens extracted from friction stir welded and TIG welded plates, flat tensile samples (longitudinally and transversely) were prepared according to ASTM E-8 standard. Instron 5982 vertical tensile testing machine (100 KN capacity) has been used to perform the tensile test at room temperature at constant cross-head speed with constant cross head speed of 1 mm/min.

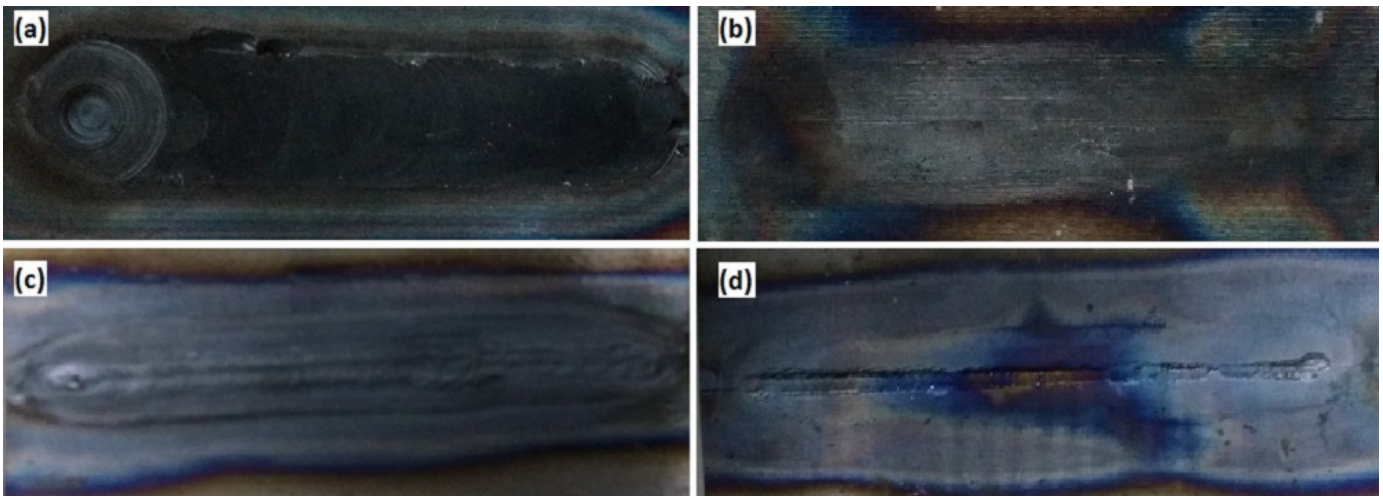

Fig. 2. Top and root of (a) & (b) FSWed butt joint and (c) & (d) Autogenous TIG welded butt join

3. Results and discussion

3.1. Microstructure characterization

Friction stir welded butt joint were produced in the experiments as shown in Fig. 2(a) and (b). The weld root was also welded properly as shown in Fig. 2(b). The used parameters for FSW are tabulated in Table. 2. The same material and same sized plates were welded by autogenous TIG welding by which sound welds were produced as shown in Fig. 2(c) and (d). The welding parameters corresponding to this TIG weld are tabulated in Table 3.

Fig. 3 shows the micrographs of stir zone, heat affected zone, base metal and their boundaries. Boundaries and other zones are shown on 200× and 500× magnifications. The micrograph of as-received base material is shown in Fig. 3(e) which shows equiaxed ferritic grains of average grain size 43.1 µm measured from line intercept method besides little colonies of pearlite. Fig. 3(a) shows the micrograph of stir zone (SZ) of FSWed butt joint which was consisted of fine ferrite, little

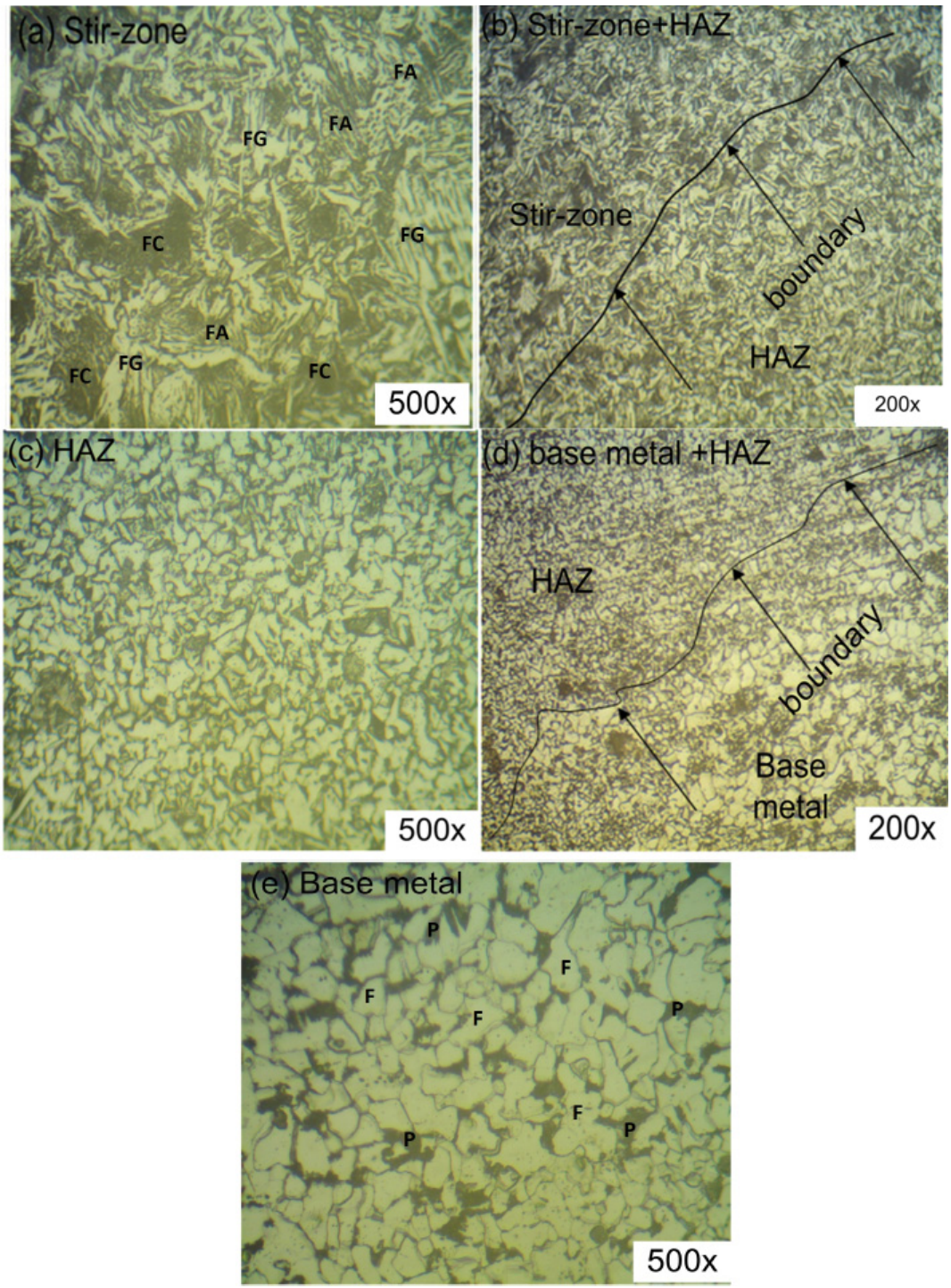

Fig. 3. Optical images of (a) stir zone at 500×, (b) stir zone and HAZ at 200×, (c) HAZ at 500×, (d) HAZ and base metal at 200× and (e) base metal at 500× for FSW

pearlite and martensite grains. The formation of equiaxed martensite in the stir zone attributed to high hardness and strength to the weld joint as compared to base metal. Theoretically, the stir zone in friction stir welding experiences thermo-mechanical cycle by heating and stirring with tool. Strain gradient is an important parameter which decreases from the contact of tool with shoulder towards the root. So, in SZ, material away from shoulder refines [12]. Material is hot worked in center during the tool interaction and due to heat generation by friction, it reaches in austenitizing temperature range, which gives appreciable grain growth. The three phases present in stir zone are: FG – grain boundaries ferrite, FA – aligned ferrite and FC – ferrite carbide aggregate (fine pearlite). Fig. 3(c) shows micrographs of heat affected zone of FSW, which has grain size 25.4 μm, measured from line intercept method. Theoretically, all solid state phase transformation like recrystallization, grain growth, tempering, annealing, phase transition, occur in HAZ of weld of steels. In case of FSW, HAZ does not experience any appreciable deformation which is nearly similar to HAZ of arc welds. Since, from fusion zone to base, peak temperature decreases; so, coarse grains are obtained near fusion line. Fig. 3(b) shows the boundary between stir zone and HAZ and Fig. 3(d) shows the boundary between HAZ and base metal at 200× magnification. It is clearly observed that the FA – aligned ferrite is absent after the boundary in Fig. 3(b). In Fig. 3(d), grains become finer from grains of HAZ near weld boundary, due to attaining lower peak temperature.

Fig. 4 shows the optical micrographs of weld zone and HAZ of TIG welded mild steel butt joint. Weld metal zone consisted of finer grains than base because of melting and solidification. Similarly, HAZ experiences the thermal cycle after reaching in austenitizing temperature zone during welding that resulted formation of coarse grains near fusion line and it becomes finer during moving towards base-HAZ boundary. In weld fusion zone, columnar grains are clearly seen.

3.2. XRD analysis

The XRD pattern for base metal, TIG weld zone and friction stir welded zone are shown in Fig. 5. In XRD analysis, the height of peaks represents the intensity in CPS (counts per second). In XRD pattern of structural steel base material, the presence of ferrite, cementite and martensite is confirmed as shown in Fig. 5(a). By using the maximum value of peak intensities, the phase analysis has been done in detail. As shown in XRD pattern of base metal, there is ferrite and cementite (Fe_3C) which confirms the presence of α-ferrite and some colonies of pearlite (ferrite+ cementite) in base. While in weld zone of FSW, presence of finer ferrite (at first and third peak), cementite (at first and second peak) and some martensite (at all three peaks) is confirmed as shown in diffractograph Fig. 5(c). Similarly, in TIG weld zone, there is martensite and ferrite on both two peaks as shown in diffractograph Fig. 5(b). Martensite presence confirms rapid cooling and solidification during fusion welding.

Table 5 shows the summary of obtained phases in XRD analysis, its structure and respective lattice parameters ($\dot{A}$). Ferrite, cementite and martensite have cubic, orthorhombic and tetragonal lattice structure respectively. Due to the tetragonal lattice structure of martensite, weld zone hardness is more than base which consists ferrite and pearlite (ferrite + cementite).

Peelamedu et al. [13] and Pandey et al. [14,15] suggested a method to find normalized intensity ratio (NIR) of phase present in both weld zone and base. On the basis of given method, NIR of a particular phase α is calculated by the following equation.

$$\left(NIR\right)_{\alpha} = \frac{I_1 - I_{back}}{I_1 + I_2 + I_3 - 3I_{back}} \tag{8}$$

where, I_1, I_2 and I_3 are the intensities of ferrite, cementite and martensite, respectively recorded in XRD analysis and I_{back} is the back ground intensity.

Calculated values of different phases obtained in XRD spectrum are tabulated in Table 6 which gives the comparison

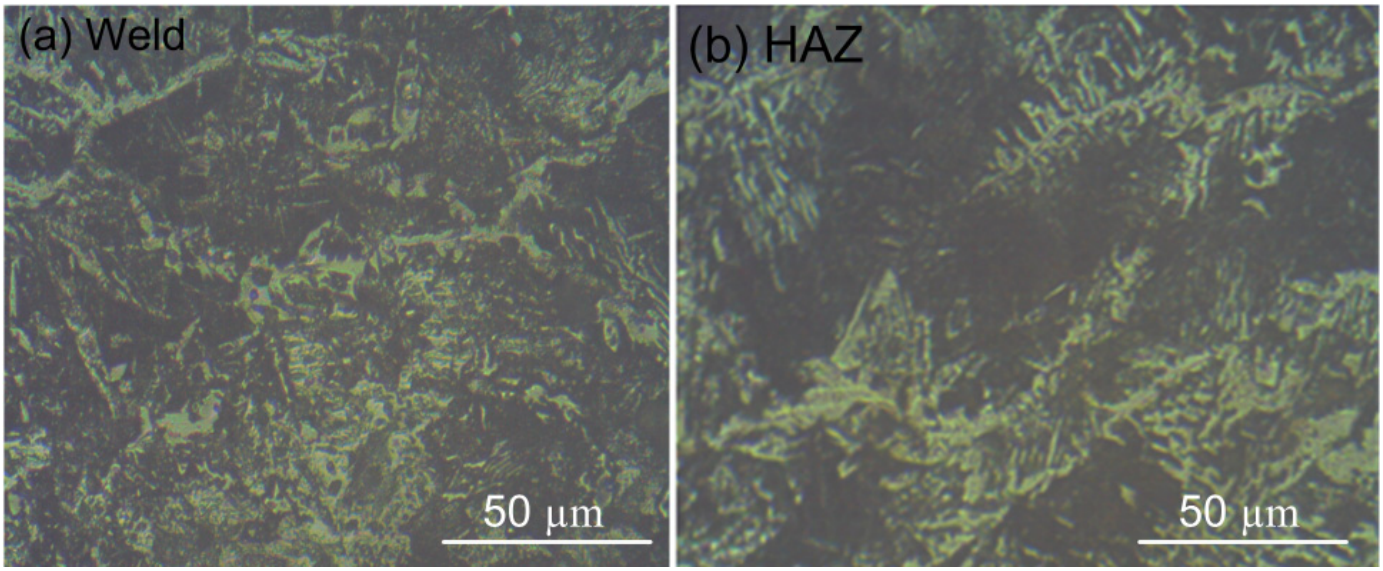

Fig. 4. Optical images of TIG weldment: (a) weld zone (b) HAZ

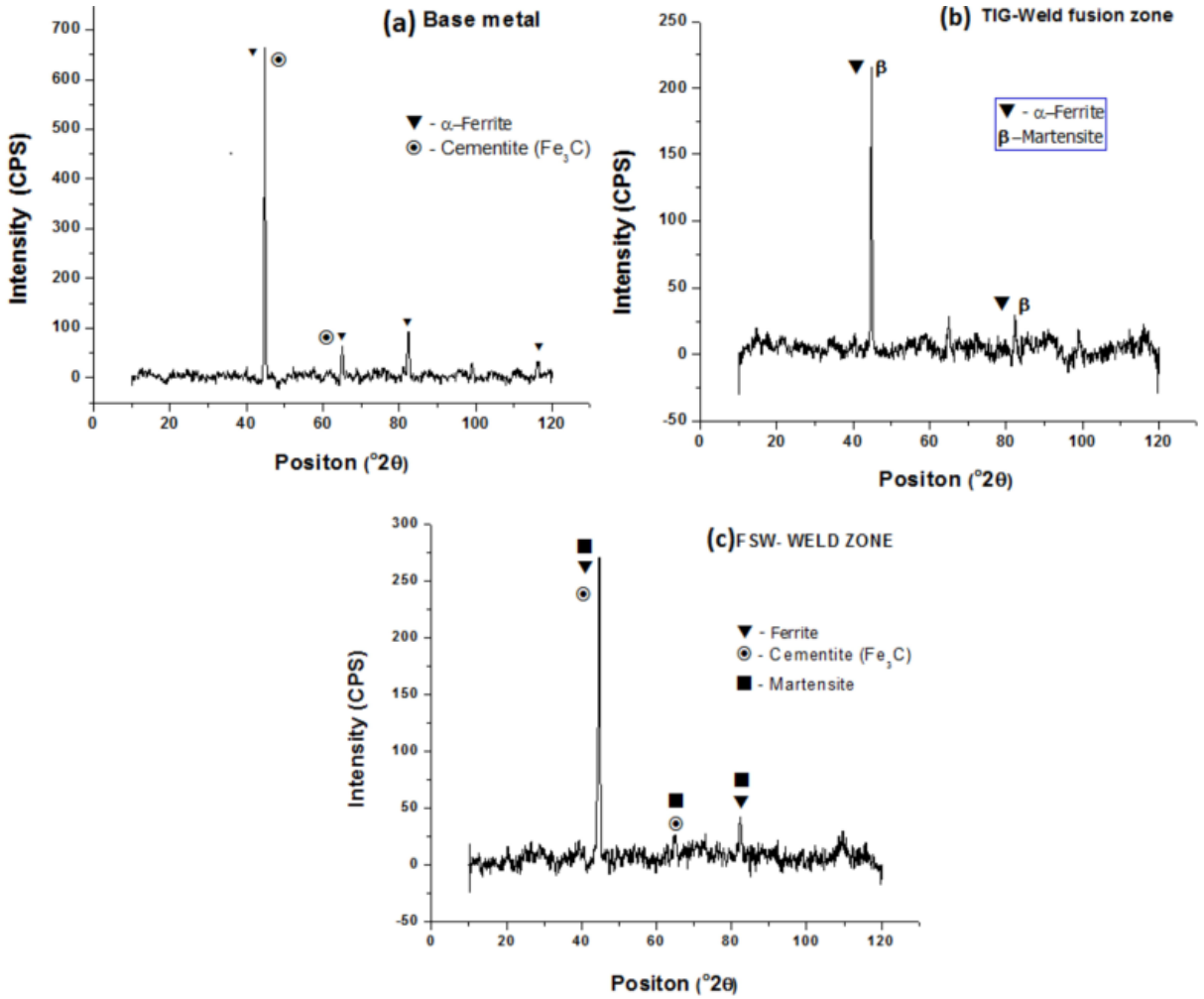

Fig. 5. Diffractograph of mild steel (a) as received base metal, (b) weld fusion zone of TIG and (c) weld zone of FSW

TABLE 5

Structure and lattice parameters of phase identified in XRD analysis

S. No.	Joint type	Phase detected	Structure	Lattice parameter (*A*)
1	Base metal	Ferrite	Cubic	a = 2.8664 b = 2.8664 c = 2.8664
		Cementite	Orthorhombic	a = 4.5100 b = 5.0400 c = 6.7300
2	TIG – weld	Ferrite	Cubic	a = 2.8664 b = 2.8664 c = 2.8664
		Martensite	Tetragonal	a = 2.8460 b = 2.8460 c = 3.0530
3	FSW – weld	Ferrite	Cubic	a = 2.8664 b = 2.8664 c = 2.8664
		Martensite	Tetragonal	a = 2.8460 b = 2.8460 c = 3.0530
		Cementite	Orthorhombic	a =4.5100 b = 5.0400 c = 6.7300

between FSW weld, TIG weld and base metal. On a single peak in XRD spectrum, there is a considerable overlapping of more than one phases which causes some difficulties in calculation of NIR values.

TABLE 6

Calculated NIR (%) for obtained phases in different joint types

S. No.	Joint type	Phase	I_1	I_2	I_3	I_{back}	NIR (%)
1	Base metal	Ferrite	662		—	0	50
		Cementite		662	—	0	50
2	TIG – weld	Ferrite	223		—	0	50
		Martensite		—	223	0	50
3	FSW – weld	Ferrite	278		—	0	33.33
		Martensite		—	278	0	33.33
		Cementite		278	—	0	33.33

3.3. Hardness

In transverse direction at the center of weld joint, the micro-hardness was measured at 1 mm interval, as shown in Fig. 6(a-b). The variation in hardness value for TIG weld joint is shown in Fig. 6(a). The hardness of as-received material was approximately

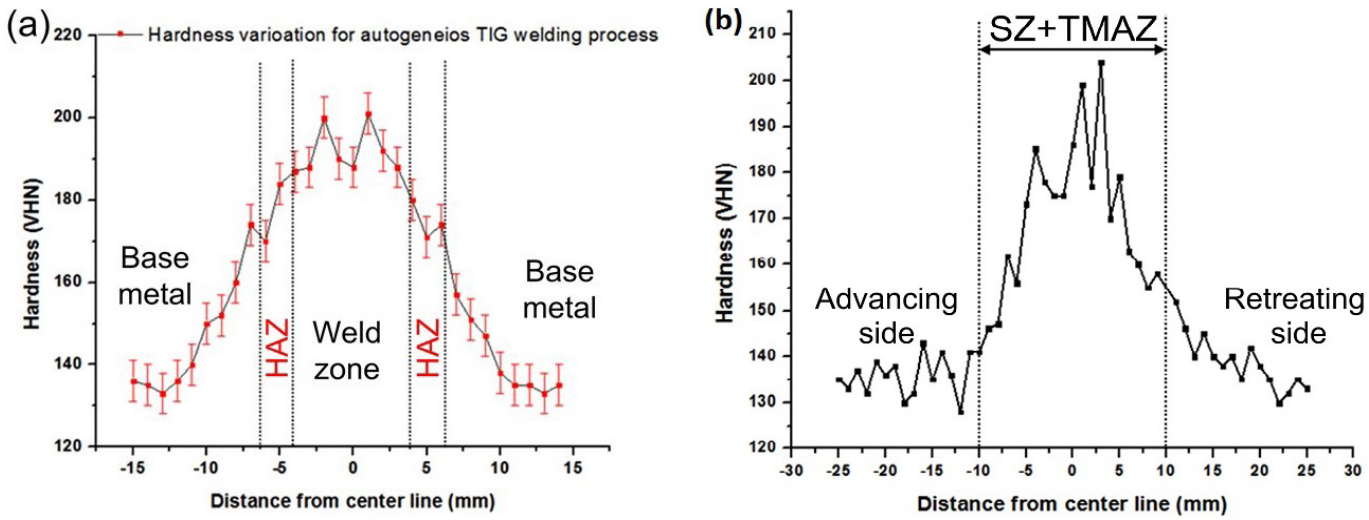

Fig. 6. Hardness profile along transverse direction in; (a) autogenous TIG welding and (b) FSW

135±7 HV. The maximum hardness achieved was 200 HV. In weld fusion zone, hardness varied from 180-200 HV while in heat affected zone varied from 170-180 HV which was lower than the weld fusion zone. These hardness results are partially in good agreement with literature. However, Boumerzoug et al. [11] have reported the hardness range of 178-250 HV for the SMAW joint.

For FSW, the hardness was measured from advancing side towards base metal to observe the differences between different zones of FSW as plotted in Fig. 6(b). The maximum hardness was obtained in the stir zone as 204 HV. Nearly 20 mm wide weld was obtained which has been the region of stir zone and thermomechanically heat affected zone in which hardness varied from 141 HV-204 HV. In HAZ region, little more hardness was obtained than for advancing side than retreating side. This might be due to little higher heat input in advancing side than retreating. The similar hardness range for the FSW joint was also reported by the Sharma et al. [9].

Along the thickness, hardness was recorded in friction stir welded and TIG welded samples. Fig. 7 shows the hardness profile from top to bottom with 0.5 mm distance between two successive indentations. In friction stir welding hardness is of decreasing nature from 200 HV to 180 HV. At the top of the weld, hardness is more due to the contact of tool shoulder and work surface. The mechanical strain was more on top due to which aligned ferrite formed. At root portion of the weld, hardness was observed to be lower. It is due to the less mechanical strain which depends on distance between tool shoulder and work material. In autogenous TIG welding of mild steel butt joint, hardness at the top is lower than at the bottom surface.

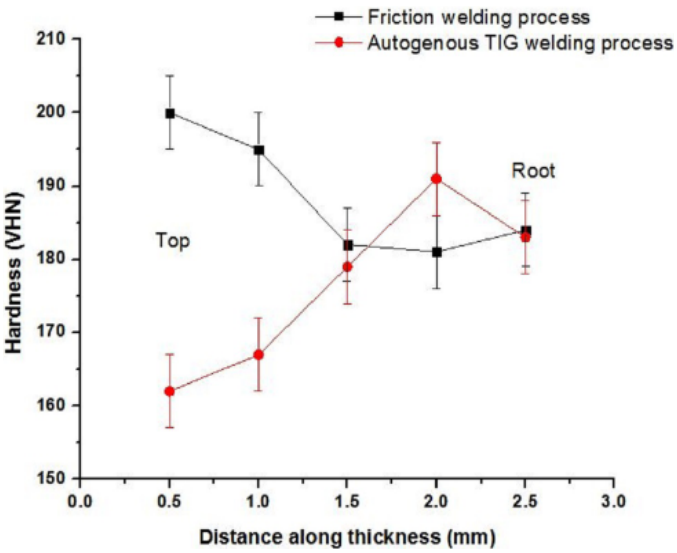

Fig. 7. Hardness profile along thickness in FSWed and TIG welded samples

3.4. Tensile properties

Tensile strength has been compared in both longitudinal (all weld) and transverse direction. In the transverses weld samples, the fracture is occurred in base material zone invariably. So, for getting the strength of weld; all weld samples are extracted in the longitudinal direction. The strength of low carbon steel is usually decided by the yield strength, thus yield strength is tested. The comparison of tensile properties between base, TIG weld and friction stir weld has been done in both orientation; longitudinal and transverse. The joint type with the orientation, tensile strength, yield strength (ductility), percentage elongation, fracture point and joint efficiency are tabulated in Table 7. Tensile strength of TIG weld is highest in transverse orientation and it is followed by base and then friction stir weld. The engineering stress-strain curve and true stress-strain curve for transverse weld and longitudinal weld including base metal is depicted in Fig. 8(a-b) and Fig. 9(a-b). Compared to base metal, the yield strength of fusion zones of TIG welded and friction stir welded joints are increased and this increment is significantly more in friction welded than TIG welded. It can be seen that the elongation in base metal specimen is more than friction stir welded and TIG welded transverse specimen. FSWed has minimum

elongation due to the presence of thermo-mechanical forces. The elongation in TIG is more than FSW because of melting and solidification and only thermal involvement. It is finalized that the ductility decreases in order from base metal then fusion welding and then solid state welding. Maximum true stress was measured to be 683±12 MPa for longitudinal TIG weld. The true stress value for different weld and base metal is depicted in Table 7. Maximum variation in engineering stress and true stress value was noticed for base metal and longitudinal weld. For TIG transverse, the true stress was measured to be 8.9% more than the engineering stress while for TIG longitudinal weld, it was 13.45%.

The serrations was also noticed for both longitudinal and transverse tensile test graph, as shown in Fig. 8(a) and Fig. 9(a). Serration is defined as the abrupt drop in stress value below the general flow curve. The serrations flow was mainly noticed at high temperature are low strain rate. In the low strain rate region, serrations is characterized as repeated appearance of discontinuities in the strain stress curve of deforming alloy and known as Portevin-Le Chatelier (PLC) effect. Serrations are mainly noticed at high temperatures and low strain rates. However, sometimes serrated flow with few serrations was observed at room temperature and low strain rate [16]. At low strain rate, interaction between solutes atmosphere and dislocations may be dominant. It was presumed that the dislocations are aged by the solutes carbon from initial straining. When number of dislocation reach a critical moving velocity, they can break away from the carbon solutes atmosphere [17,18]. This resulted a rapid mobile dislocations and hence the abrupt change in stress and finally lead to serrations.

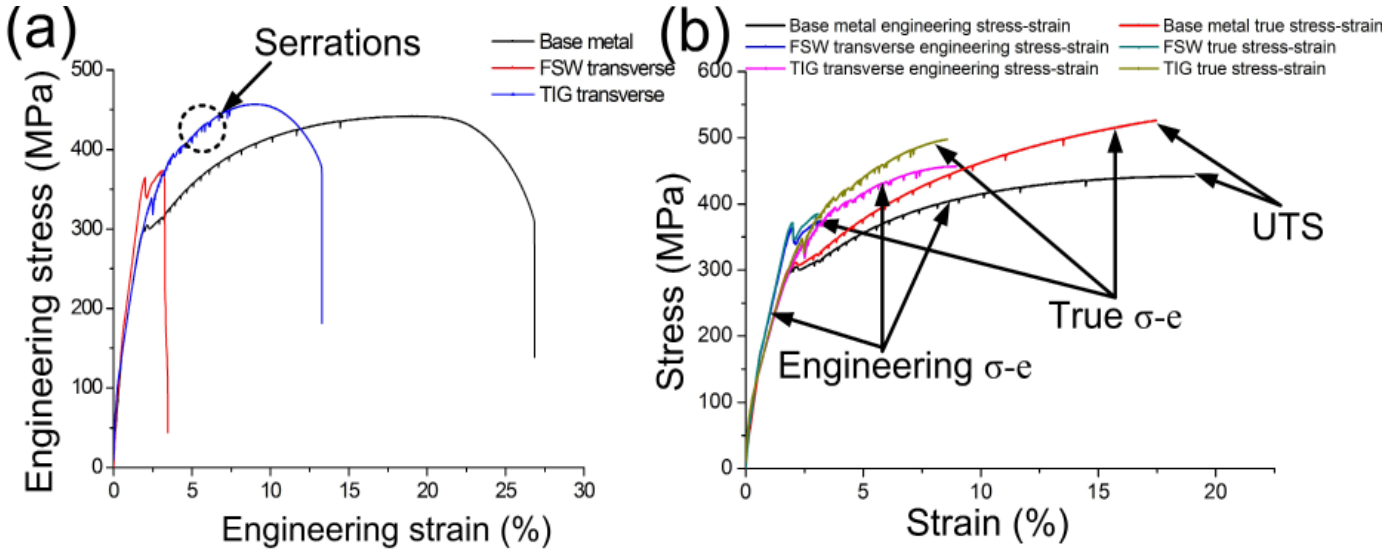

Fig. 8. (a) Engineering stress-strain curve for transverse weld sample with serrations mark, (b) Comparison of engineering stress-strain and true stress-strain curve

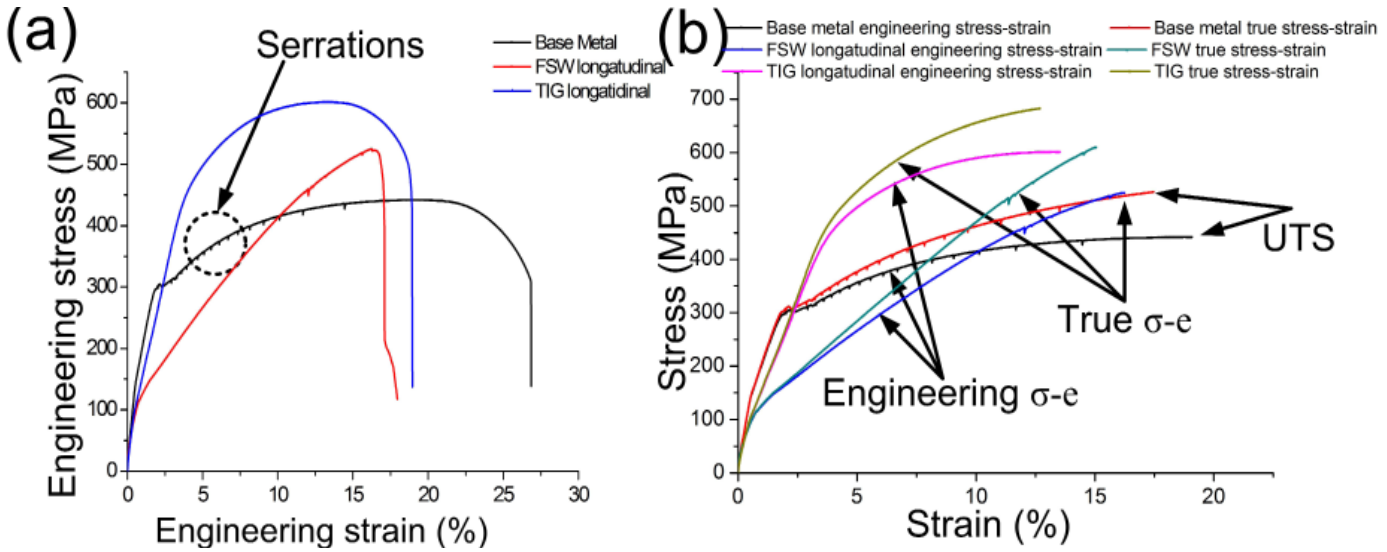

Fig. 9. (a) Engineering stress-strain curve for longitudinal weld sample with serrations mark, (b) Comparison of engineering stress-strain and true stress-strain curve for longitudinal weld

TABLE 7

Comparison of tensile properties of base and welded joints in different orientation

S. No.	Joint type	Fracture location	Ultimate tensile strength (MPa)	Yield strength (MPa)	True stress (MPa)	% elongation
1	Base metal		442±10	300±12	526±10	37±4
2	FSW longitudinal orientation	Gauge length	525±8	275±9	610±8	28±3
3	TIG longitudinal orientation	Gauge length	602±12	430±10	683±12	25±2
5	FSW transverse orientation	Weld	380±5	320±6	390±5	10±2
6	TIG transverse orientation	Base area	457±9	325±10	498±9	22±4

In FSW transverse tensile specimen, the fracture occurred from the weld fusion zone. The most probable reason for the failure occurred in weld zone is less penetration of stirring up to the root. While in TIG welded transverse specimen, failure occurred in base metal portion which confirms the higher strength of weld zone due to fine columnar grains and presence of martensite structure.

3.5. Comparison of residual stress

The residual stresses have been calculated from formulations of ASTM E837 in which calibration coefficients and other constants are used. Measured residual stresses at different locations are shown in Table 8. The magnitude of longitudinal stress at weld line of TIG welded plate is more than friction stir welded joint, having difference of 48 MPa and both are having tensile nature (Fig. 10). The obtained magnitude and nature of residual stress match theoretically for both fusion and solid state welding. Thus, it is finalized that the residual stress is more in fusion welding process than solid state friction stir welding process. By observing the comparison between the residual stresses between TIG and FSW, residual stress is 25.66% less in FSW than TIG weld.

TABLE 8

Measured residual stresses and its nature at different locations of weld

S. No.	Residual stress measurement locations	Measured longitudinal stress (MPa)	Stress nature
1.	TIG weld line	187±25	Tensile
2.	TIG heat affected zone	118±20	Tensile
3.	FSW weld line	139±24	Tensile
4.	Base metal	15±5	Compressive

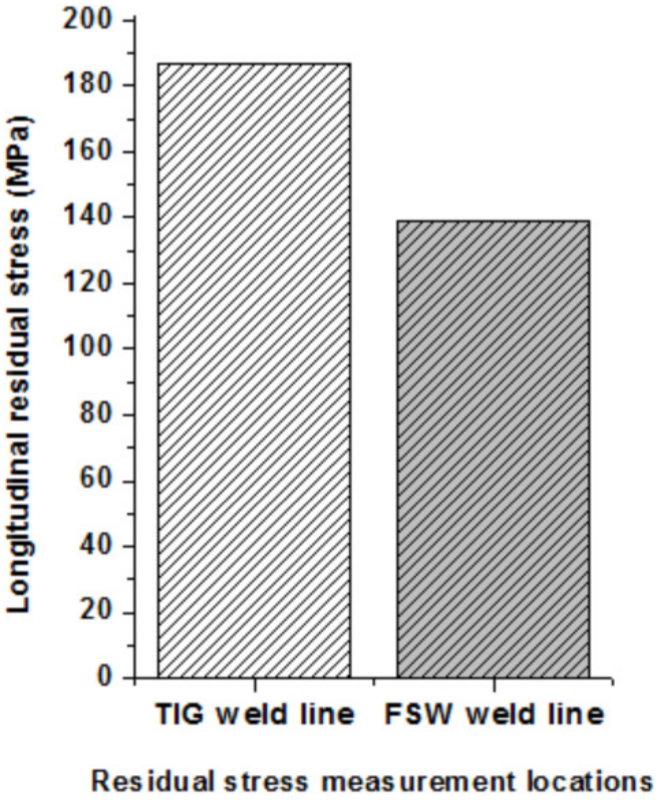

Fig. 10. Difference of longitudinal residual stress between TIG weld line and FSW weld line

The measured residual stresses corresponding to place are graphed in Fig. 11(a) and (b). For TIG weld, longitudinal residual stress is measured at weld centerline and HAZ. At weld, it is higher than HAZ and of the tensile nature. In friction stir welded plate, at the weld centerline, the residual stress is of tensile nature longitudinally which has lower value (139 MPa) than TIG. In base metal, the measured residual stress is 15 MPa (compressive), which is theoretically correct also. Base metal portion of a weld mainly has compressive nature of residual stress as shown in Fig. 11(b). Thus, it is finalized that the obtained results of residual stress are fairly match with the theoretical pattern of residual stress in arc weld and friction stir weld joints.

4. Conclusions

The following conclusions can be made from the present research work.

1) Friction stir welded structural steel butt joint of thickness 3 mm was successfully produced with rotational speed 931 rpm and welding speed 20 mm/min without defect. Defect free autogenous TIG welded structural steel butt joint of thickness 3 mm was successfully produced with 140 A welding current, 12 V welding voltage and 90 mm/min welding speed.
2) Finer ferrite formation in the stir zone and coarse as well as fine grain formation in HAZ of friction stir weld has been confirmed for structural steel butt welds. Martensite

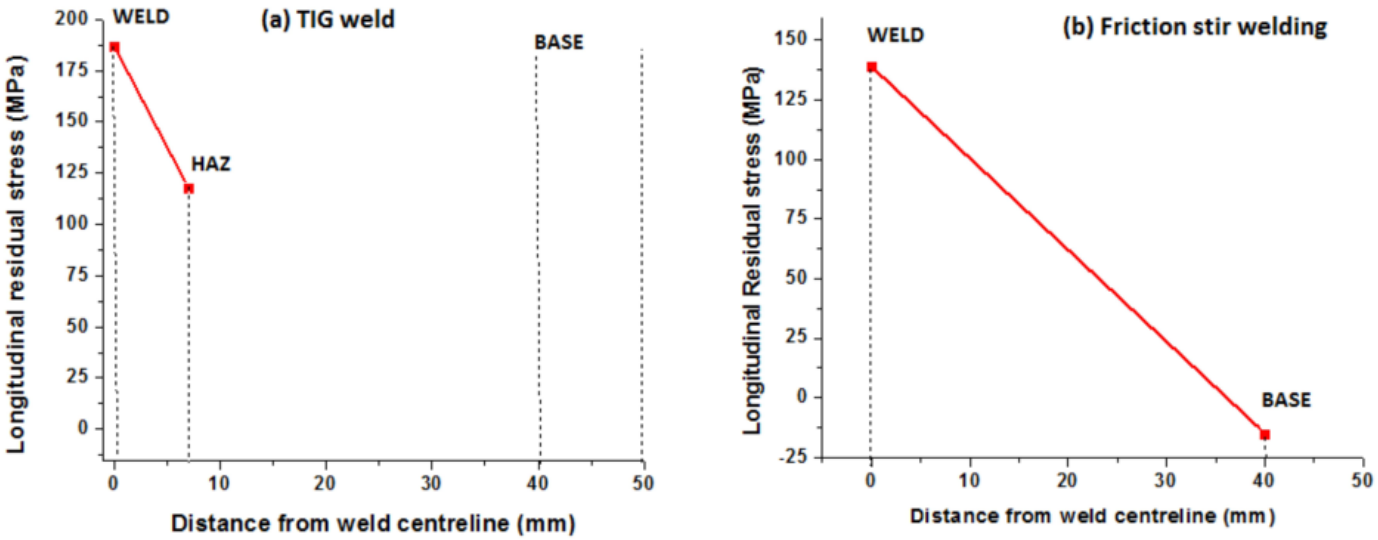

Fig. 11. Residual stresses for (a) TIG welds and, (b) Friction stir weld

formation percentage has been higher in TIG welds due to rapid melting and solidification.

3) In friction stir welds, hardness of 204 HV in stir zone was observed due to grain refinement. A similar trend was obtained in TIG weld (200 HV) due to presence of martensite.
4) In tensile test, TIG weld exhibited highest tensile strength of 457 MPa which was more than the welds produced by FSW in transverse orientation. In longitudinal orientation, TIG weld also exhibited the highest strength of 602 MPa.
5) The calibration coefficients ($\overline{A}$ and $\overline{B}$) for steel were measured to be -11.43×10^{-13} and -18.98×10^{-13} MPa^{-1}, respectively; and calibration constants (a and b) are 0.37 and 0.79, respectively. Residual stress was measured at different locations in both welds by using three element strain gauge rosette (FRS-2-11) which measured strain relaxation in transverse, longitudinal and inclined (45°) directions. The longitudinal residual stress in TIG welds was higher than FSWed plate by 48 MPa (tensile). Base plate has compressive nature of residual stress.

REFERENCES

[1] W. Zinn, B. Scholtes, Handbook of residual stress and deformation of steel, 391(2013).
[2] N.S. Rossini, M. Dassisti, K.Y. Benyounis , A.G. Olabi, Materials & Design **35**, 572 (2012).
[3] A. Giri, C. Pandey, M.M. Mahapatra, K. Sharma, P.K. Singh, Measurement **65**, 41 (2015).
[4] Vishay Precision Group, Tech Note TN **503**, 19-33 (2010).
[5] C.M. Chen, R. Kovacevic, Machine Tools & Manufacture **43**, 1319 (2003).
[6] Z.M. Hu, P. Blackwell, J.W. Brooks, Residual stress in friction stir welding, in ABAQUS Users' conference, 2004, UK.
[7] L. Fratini, S. Pasta, Journal of Materials: Design and Applications 224, 149 (2010).
[8] M.T. Milan, J.R. Tarpani, W.W. Bose Filho, Residual stress evaluation of AA2024-T3 friction stir welded joints, in 18th International Congress of Mechanical Engineering, 2005, p. 6-11, 2005, Ouro Preto, Minar Gerais.
[9] G. Sharma, D.K. Dwivedi, T. Indian I. Metals, 2016, DOI 10.1007/s12666-016-0876-x.
[10] T.J. Lienert, W.L. Stellwag, B.B. Grimmett, R.W. Warke, Welding Journal 1, (2003).
[11] Z. Boumerzoug, C. Derfouf, T. Baudin, Engineering **2**, 502 (2010).
[12] J. Pasupathy, IJERT **2** (11), 1558 (2013).
[13] R.D. Peelamedu, R. Roy, D.K. Agrawal, Mater. Lett. **55**, 234 (2002).
[14] C. Pandey, A. Giri, M.M. Mahapatra, Mater. Sci. Eng. A **664**, 58 (2016).
[15] C. Pandey, A. Giri, M.M. Mahapatra, P. Kumar, Met. Mater. Int. **23** (1), 148 (2017).
[16] L. Qian, P. Guo, F. Zhang, J. Meng, M. Zhang, Mater. Sci. Eng. A **561**, 266 (2013).
[17] R.C. Picu, G. Vincze, J.J. Gracio, F. Barlat, Scr. Mater. **54**, 71 (2006).
[18] F. Ozturk, H. Pekel, H.S. Halkaci, J. Mater. Eng. Perform. **20**, 77 (2011).